**Applied Physics Laboratory**

University of Washington

1013 NE 40<sup>th</sup> Street
Box 355640
Seattle, WA 98105-6698

206-543-1300
FAX 206-543-6785
www.apl.washington.edu

13 December 2017

To:     Kyle Becker, Program Manager
        Office of Naval Research (ONR 322)
        875 North Randolph Street
        Arlington, VA 22203-1995

From:   Steven Kargl

Subj:   Grant: N00014-16-1-3209
        "Target Scattering Metrics: Model-Model and Model-Data comparisons"

Encl:   (1) Final Performance/Technical Report with SF298

Enclosed please find the Final Performance/Technical Report for the project titled "Target Scattering Metrics: Model-Model and Model-Data comparisons." Distribution Statement A. Approved for public release; distribution is unlimited.

Cc:     ONR Seattle - Robert Rice and Kyoohui Beal
        Naval Research Laboratory
        DTIC
        Office of Sponsored Programs – UW Closeout
        APL-UW Grants and Contracts Closeout Coordinator

# Target Scattering Metrics: Model-Model and Model-Data comparisons

Steven G. Kargl

Applied Physics Laboratory, University of Washington, 1013 NE 40th St., Seattle WA 98105-6698
Phone: (206) 685-4677    FAX: (206) 543-6785    Email: kargl@apl.washington.edu

## ABSTRACT

The development of metrics for the comparison of data obtained from measured synthetic aperture sonar (SAS) data or from numerical models is investigated. Metrics are needed for quantitative comparisons for signals obtained from either different models, the same model with omitted physics, controlled experiments, or actual operational MCM systems. Specifically, candidate metrics for model-model comparisons are examined here with a goal to consider raw data prior to its reduction to data products, which may be suitable for input to classification schemes. The investigated metrics are then applied to model-data comparisons.

## INTRODUCTION

Metrics for quantitative comparison of acoustic color templates were considered under ONR Award N00014-14-1-0288. An acoustic color (AC) template displays target strength as a function of frequency and target-centered aspect angle. In that research, it was found that the maximum value of the magnitude of a simple 2D cross-correlation of two AC templates appeared to be an adequate metric for model-model comparisons in the absences of injected noise. Model-data comparisons suggested additional metrics were needed due to uncertainties within the measurements (e.g., signal-to-noise ratio) or due to the acquisition of only a limited section of a full 360° acoustics color template. During FY15, target isolation techniques were applied to the TREX13 data, which led to isolated target signatures for more than 25 targets. For each target, the isolated signatures were combined to form a pseudo-circular SAS data and an ultimately AC template. Instead of working with these AC templates, the current research worked directly with isolated target signatures.

The metrics considered here are based on an extension of Parseval's theorem to comparisons between signals from possibly different targets or the same target in different orientations. Let a time-dependent isolated scattered signal be denoted by $s_i(t)$ with time $t$. Its frequency-domain Fourier transform is $S_i(f) = F\{s_i(t)\}$ with frequency $f$. The subscript here denotes the $i$th signal from a collection of scattered signals. The total power in a signal is the same whether computed in the time domain or the frequency domain. Parseval's theorem states that a signal satisfies

$$\int_{-\infty}^{\infty} |s_i(t)|^2 dt = \int_{-\infty}^{\infty} |S_i(f)|^2 \, df. \tag{1}$$

To exploit Eq. (1), it is convenient to write $|s_i|^2 = |s_i||s_i| = s_i s_i^*$ where the last equality introduces the complex conjugate $s_i^*$ (and likewise for the right-hand-side of Eq. (1)). Rewriting Eq. (1), where the integrand of is replaced by its complex product, one has

$$\int_{-\infty}^{\infty} s_i(t)s_i^*(t)dt = \int_{-\infty}^{\infty} S_i(f)S_i^*(f) \, df. \tag{2}$$

Now, consider a possibly second signal and define the "pseudo-" total power defined as

$$\langle i,j \rangle = \int_{-\infty}^{\infty} s_i(t)s_j^*(t)dt \tag{3}$$

or

$$\langle i,j \rangle = \int_{-\infty}^{\infty} S_i(f)S_j^*(f)\,df. \tag{4}$$

If $i$ is the same as $j$, then Eqs. (3) and (4) reduce to Parseval's theorem. To compare $\langle i,j \rangle$, to the results of cross-correlation $corr(s_i, s_j) = F^{-1}\{S_iS_j^*\}$, define the normalized result

$$[i,j] = \frac{\langle i,j \rangle}{\sqrt{\langle i,i \rangle \langle j,j \rangle}} \tag{5}$$

where the normalized cross-correlation is similar to Eq. (5) with $\langle i,j \rangle$ understood to be the maximum value in the magnitude of an inverse Fourier transform of the product of $S_i(f)$ and $S_j^*(f)$.

To examine the consequences of Eqs. (3) and (4), the target-in-the-environment response (TIER) model is used to simulate the scattering from targets under a number of conditions. The environment is taken to be that of TREX13 with water above a medium-sand sediment. The density and sound speed of water are $\rho = 1000$ kg/m³ and $c = 1530$ m/s; while, the sediment's density, sound speed, and loss parameter are $\rho = 2000$ kg/m³, $c = 1694$ m/s, and $\delta = 0.008$, respectively. The source and receiver are co-located at $z = 4$ m above the water-sediment boundary, and targets were placed at horizontal ranges of 10 and 12 m. The signal transmitted by the source is a linear-frequency-modulated (LFM) chirp with a 16 kHz carrier frequency and 30 kHz of bandwidth. The magnitudes of the pulse-compressed scattered signal are displayed in Figure 1 where the targets are a solid aluminum sphere and cylinder. The radii of the targets are 0.1524 m and the cylinder is 0.61 m in length. The source, receiver, and cylinder are oriented to give broadside scattering. TIER simulations were performed for free-field scattering where only the direct path (i.e., in the TIER Path 1) is included and for proud targets where four ray paths are included. Thus, eight signals were generated.

To facilitate discussion of these signals, a labeling scheme is required. For signals associated with the spherical or cylindrical targets, the initial letter in the label is either "S" or "C". The next number indicates the number of paths included in a simulation; for example, "S1" is for the spherical target and only direct path scattering. Finally, the last three characters indicate the horizontal range to the target, e.g., "h10". These labels are used in the following tables.

Table 1 contains the values computed from Eq. (5) where the cross-correlations of the signals are computed. Entries in the table are color-coded to aid in discussing the results. First, the diagonal entries are unity as expected from the normalization imposed by Eq. (5). The largest non-diagonal entries (red) occur for scattering in the free-field, where either the spherical or cylindrical target is simply translated by 2 meters. An interesting result is that the scattered signal from the proud spherical target at 10 m (S4h10) and at 12 m (S4h12) appear to have fairly high correlations with the cylindrical target at the same distance (green). This is a consequence of the radii of the targets and the cylinder is at a broadside orientation, which means the phase delays for paths 2, 3, and 4 are identical for the sphere and cylinder.

|       | S1h10 | S1h12 | S4h10 | S4h12 | C1h10 | C1h12 | C4h10 | C4h12 |
|-------|-------|-------|-------|-------|-------|-------|-------|-------|
| S1h10 | 1.000 | 0.993 | 0.541 | 0.490 | 0.745 | 0.741 | 0.436 | 0.447 |
| S1h12 |       | 1.000 | 0.535 | 0.488 | 0.738 | 0.745 | 0.437 | 0.458 |
| S4h10 |       |       | 1.000 | 0.550 | 0.768 | 0.774 | 0.822 | 0.476 |
| S4h12 |       |       |       | 1.000 | 0.644 | 0.637 | 0.571 | 0.828 |
| C1h10 |       |       |       |       | 1.000 | 0.991 | 0.742 | 0.650 |
| C1h12 |       |       |       |       |       | 1.000 | 0.748 | 0.637 |
| C4h10 |       |       |       |       |       |       | 1.000 | 0.633 |
| C4h12 |       |       |       |       |       |       |       | 1.000 |

Table 1. Values estimated from Eq. (5) where cross-correlations are computed. By construction, the table is symmetric, so lower triangular elements are omitted. The direct path scattering from the spherical or cylindrical target at a 10 m shows a high cross-correlation (red) with the same target at its 12 m horizontal range.

Table 2 is evaluated from Eqs. (3) and (5) with the additional constraint that only real signals are used, i.e., $s_i s_j^* = \Re(s_i)\Re(s_j)$. That is, the complex conjugate of the signal is not used. In Table 2, the red entries highlight very small numbers. These can easily be understood from inspection of Figure 1, which shows that any scattered signal for a target at 10 m is nearly quiescent after 2 ms and hence its multiplication with a signal for a target at 12 m is negligible.

|       | S1h10 | S1h12 | S4h10 | S4h12 | C1h10 | C1h12 | C4h10 | C4h12 |
|-------|-------|-------|-------|-------|-------|-------|-------|-------|
| S1h10 | 1.000 | 0.002 | 0.541 | 0.003 | 0.628 | 0.002 | 0.285 | 0.002 |
| S1h12 |       | 1.000 | 0.002 | 0.411 | 0.007 | 0.628 | 0.000 | 0.179 |
| S4h10 |       |       | 1.000 | 0.000 | 0.318 | 0.003 | 0.657 | 0.003 |
| S4h12 |       |       |       | 1.000 | 0.003 | 0.217 | 0.001 | 0.640 |
| C1h10 |       |       |       |       | 1.000 | 0.002 | 0.456 | 0.014 |
| C1h12 |       |       |       |       |       | 1.000 | 0.005 | 0.361 |
| C4h10 |       |       |       |       |       |       | 1.000 | 0.008 |
| C4h12 |       |       |       |       |       |       |       | 1.000 |

Table 2. Values estimated from Eq. (5) where Eq. (3) is used for $\langle i, j \rangle$. By construction, the table is symmetric, so the lower triangular elements are omitted. The light blue entries are a result that the direct path scattering align and thus are re-enforced through the multiplication.

Table 3 is evaluated from Eqs. (3) and (5) with the additional constraint that the magnitudes of the signals are used. That is, the complex conjugate of the signal is not used. In Table 3, the red entries again highlight small numbers. These can easily be understood from inspection of Figure 1, which shows that any scattered signal for a target at 10 m is nearly quiescent after 2 ms and hence its multiplication with a signal for a target at 12 m is nearly zero. Note the larger values observed in

Table 3 than in Table 2 are a result of the conversion of the integrals to discrete summations where the summands for Table 3 are always positive while some of the summands for Table 2 are negative.

|       | S1h10 | S1h12 | S4h10 | S4h12 | C1h10 | C1h12 | C4h10 | C4h12 |
|-------|-------|-------|-------|-------|-------|-------|-------|-------|
| S1h10 | 1.000 | 0.019 | 0.630 | 0.018 | 0.753 | 0.019 | 0.488 | 0.018 |
| S1h12 |       | 1.000 | 0.018 | 0.592 | 0.024 | 0.756 | 0.021 | 0.463 |
| S4h10 |       |       | 1.000 | 0.018 | 0.472 | 0.017 | 0.775 | 0.019 |
| S4h12 |       |       |       | 1.000 | 0.022 | 0.446 | 0.019 | 0.787 |
| C1h10 |       |       |       |       | 1.000 | 0.022 | 0.559 | 0.028 |
| C1h12 |       |       |       |       |       | 1.000 | 0.021 | 0.494 |
| C4h10 |       |       |       |       |       |       | 1.000 | 0.020 |
| C4h12 |       |       |       |       |       |       |       | 1.000 |

Table 3.  Values estimated from Eq. (5) where Eq. (3) is used for $\langle i, j \rangle$.  By construction, the table is symmetric, so the lower triangular elements are omitted.  The light blue entries are a result that direct path scattering align and thus are re-enforced through the multiplication of the magnitudes.

Table 4 is evaluated from Eqs. (3) and (5).  Here, the complex conjugate of the signal is used, so Table 4 represents the time-domain Parseval's theorem result.  In Table 4, the red entries again highlight small numbers.  These can easily be understood from inspection of Figure 1, which shows that any scattered signal for a target at 10 m is nearly quiescent after 2 ms and hence its multiplication with a signal for a target at 12 m is nearly zero.  The discrete summations from the conversion of the integral in Eq. (3) is a coherent summation of complex summands.  The scattering geometries for the sphere and cylinder were constructed to give essentially the same path lengths for all paths, and the broadside orientation of the cylinder yields a specular scattering return that is similar to the specular return from

|       | S1h10 | S1h12 | S4h10 | S4h12 | C1h10 | C1h12 | C4h10 | C4h12 |
|-------|-------|-------|-------|-------|-------|-------|-------|-------|
| S1h10 | 1.000 | 0.024 | 0.680 | 0.022 | 0.911 | 0.025 | 0.600 | 0.022 |
| S1h12 |       | 1.000 | 0.022 | 0.627 | 0.029 | 0.911 | 0.025 | 0.554 |
| S4h10 |       |       | 1.000 | 0.022 | 0.599 | 0.022 | 0.941 | 0.023 |
| S4h12 |       |       |       | 1.000 | 0.031 | 0.543 | 0.025 | 0.951 |
| C1h10 |       |       |       |       | 1.000 | 0.025 | 0.609 | 0.032 |
| C1h12 |       |       |       |       |       | 1.000 | 0.024 | 0.531 |
| C4h10 |       |       |       |       |       |       | 1.000 | 0.025 |
| C4h12 |       |       |       |       |       |       |       | 1.000 |

Table 4.  Values estimated from Eq. (5) where Eq. (3) is used for $\langle i, j \rangle$.  By construction, the table is symmetric, so the lower triangular elements are omitted.  The light blue entries are a result that direct path align and thus are re-enforced through the multiplication of the magnitudes.

the sphere.   In addition, the dominate surface elastic wave is associated with a Rayleigh wave resonance in the frequency range considered, and repeated circumnavigations of the surface wave on the sphere and cylinder traverse a similar path length.  Hence, the coherent processing enhances the comparisons of the scattering from the sphere and cylinder, which leads to the blue entries in Table 4.

The final result for the frequency-domain Parseval's theorem is computed from Eqs. (4) and (5), and are tabulated in Table 5.  One immediately sees that many of the entries exceeds 0.900.  This is simply a manifestation of Eq. (5) summing up the acoustic energy in all frequencies without using phase information; whereas the cross-correlation results in Table 1 use the maximum value from the magnitude of the cross-correlation (i.e., the amplitude where $s_i$ and $s_j$ have the best match).  For finite duration scattered time signals, the frequency-domain Parseval's theorem may have limits.

|        | S1h10 | S1h12 | S4h10 | S4h12 | C1h10 | C1h12 | C4h10 | C4h12 |
|--------|-------|-------|-------|-------|-------|-------|-------|-------|
| S1h10  | 1.000 | 1.000 | 0.902 | 0.908 | 0.900 | 0.900 | 0.787 | 0.806 |
| S1h12  |       | 1.000 | 0.902 | 0.908 | 0.900 | 0.900 | 0.787 | 0.806 |
| S4h10  |       |       | 1.000 | 0.876 | 0.924 | 0.924 | 0.919 | 0.834 |
| S4h12  |       |       |       | 1.000 | 0.916 | 0.916 | 0.825 | 0.919 |
| C1h10  |       |       |       |       | 1.000 | 1.000 | 0.908 | 0.928 |
| C1h12  |       |       |       |       |       | 1.000 | 0.908 | 0.928 |
| C4h10  |       |       |       |       |       |       | 1.000 | 0.860 |
| C4h12  |       |       |       |       |       |       |       | 1.000 |

Table 5.  Values estimated from Eq. (5) where Eq. (4) is used for $\langle i, j \rangle$.  By construction, the table is symmetric, so the lower triangular elements are omitted.  The light blue entries are a result that direct path align and thus are re-enforced through the multiplication of the magnitudes.

In the development of Tables 1-5, only eight scattered signals from two targets were considered. The scattering geometry and targets used for the comparison for selected as these are often use in benchmark comparisons (i.e., spherical target or finite-length cylinder at broadside).  The sequel, the metrics developed in Eqs. (2) - (5) as well as 2D cross-correlation are applied to slices of data from either TIER-based SAS simulations or measurements (i.e., TREX13 data).  A slice of data consists of 81 signals with a 0.5° spacing along a linear SAS path.  The signals are 30 ms in duration and a time offset is chosen based on an estimate of the earliest expected arrival from a roundtrip, time-of-flight calculation.

**WORK COMPLETED**

A.   Description of TREX13 Data:

The TREX13 data were collected by scanning a sonar tower along a straight 42-m rail.  Targets were placed at horizontal ranges from 5 to 40 m in 5 m increments.  Table 6 contains the ranges where a given target had been placed during TREX13.  For an axially symmetric target such as a water-filled, 155-mm howitzer at a given location, the target was rotated from −80° (tail towards the rail) to 80° (nose towards the rail) in 20° increments.  For a non-axially symmetric target, a complete target

rotation results in 18 passes of the sonar tower along the rail to collect SAS data sufficient for a complete AC template. After matching-filtering with a replica of the transmitted signal, pulse-compressed and calibrated target signatures were isolated. Nine linear SAS data were combined into pseudo-CSAS data, which required processing to mitigate range-migration. The pseudo-CSAS data are then converted to an AC template. The current research steps back from the pseudo-CSAS data to directly use the isolated target signatures. This then yields 711 sets of data for proud targets and 144 sets of data for partially buried targets. Only the proud target data are used here. For a given run along the rail, 1600 pings at a 2.5 cm spacing are recorded with a 100 kHz sample rate for a duration of 80 ms. Thus, the size of a SAS data set is 1600×8000. To make the data manageable, it is decimated by selecting those pings that correspond to target-centered angular values in the range ±20° in 0.5° increments (i.e., 81 pings are used). The data are also reduced to a 30 ms segment by setting a time offset based on a time delay for closest approach to a target. These restrictions led to a reduction in the size of data to an 81×3000 slice. Figure 2a depicts the nine slices of data for target17 in Table 6, which is a proud 2:1 solid aluminum cylinder.

| Target | Range | Target | Range | Target | Range | Target | Range |
|--------|-------|--------|-------|--------|-------|--------|-------|
| tgt01 | 35 | tgt09 | 10, 15, 20, 35 | tgt16 | 15, 25, 30 | tgt23 | 5, 15, 20 |
| tgt02 | 35 | tgt10 | 20, 25, 30 | tgt17 | 10 | tgt24 | 5, 15, 20 |
| tgt03 | 35 | tgt11 | 10, 20, 25, 35 | tgt18 | 15 | tgt25 | 5, 15, 20, 25 |
| tgt05 | 25, 30, 40 | tgt12 | 15 | tgt19 | 20 | tgt28 | 15, 25, 30 |
| tgt06 | 25, 35, 40 | tgt13 | 15, 25, 35 | tgt20 | 10, 15 30, 40 | tgt29 | 15, 20, 35 |
| tgt07 | 30, 35, 40 | tgt14 | 15, 20, 25 | tgt21 | 10, 15, 25, 30 | tgt30 | 5, 15, 20 |
| tgt08 | 5, 25, 30, 40 | tgt15 | 15, 20, 25 | tgt22 | 5, 20, 30, 40 | | |

Table 6. Target enumeration and the horizontal ranges for deployment during TREX13 are displayed.

B.  Description of TIER Simulations:

The target-in-the-environment response (TIER) model was used to simulate the scattering of a 1-30 kHz chirp from the nine targets listed in Table 7. The targets were placed at horizontal ranges of 5 to 40 m in 5 m increments, and at each range the targets were rotated through the same ±80° in 20° increments. The source-receiver-target geometries were set up to replicate a ±20° range with the same 0.5° sampling of the slices of TREX13 data shown in Figure 2. Signals were then generated for a 30 ms time window, which is also sampled at 100 kHz.

TIER was used in a number of simulations. First, free-field scattering from the targets was predicted by including only the direct path. Figure 2b displays the predicted pulse-compressed scattering from a 2:1 solid aluminum cylinder. Second, the scattering from the same targets lying proud on a sand sediment with environmental properties from TREX13 conditions was simulated. This includes four paths: (1) the direct path, (2) two bistatic scattering paths with a single bounce off the water-sediment interface, and (3) a backscattering path that interacts with the water-sediment interface twice. Figure 2c depicts the scattering from the same cylinder. Third, the simulations were performed for the full target response and for the target response decomposed into a rigid response and

6

an elastic response. For targets of nearly the same size (e.g., sim06 - sim09 of Table 7), their rigid responses may be quite similar, but their elastic behavior may be sufficiently different to permit a classifier to exploit the decomposition of the responses. In total, 5184 sets of simulated date were generated with the same size as the slices of TREX13 data (i.e., 81×3000).

| Target | Description of target |
|--------|----------------------|
| sim01 | 2:1 solid aluminum cylinder |
| sim02 | water-filled scuba tank without stem |
| sim03 | 155-mm howitzer, filled with air, end cap |
| sim04 | 155-mm howitzer, filled with water, end cap |
| sim05 | 155-mm howitzer, no end cap |
| sim06 | 105-mm bullet-shaped artillery shell, filled with air |
| sim07 | 105-mm bullet-shaped artillery shell, filled with water |
| sim08 | 100-mm solid aluminum replica of artillery shell |
| sim09 | 100-mm solid stainless steel replica of artillery shell |
| Table 7. Targets used in the TIER simulations for the metrics study. | |

C. Four Potential Metrics:

Four potential metrics were investigated for model-model comparisons, and then these metrics were applied to model-data comparisons. One metric utilized the 2D cross-correlation of slices of data. The other three metrics are based on total power in the element-by-element matrix product of two slices of data. Each metric is defined in the following.

The first metric is the conventional method of extracting the maximum value from the absolute value of a 2D cross-correlation of slices of data. Let $s_i(t, \theta)$ and $s_j(t, \theta)$ represent two slices in the time and target-centered angular domain. Let $S_i(f, \vartheta)$ and $S_j(f, \vartheta)$ represent the 2D Fourier transforms of $s_i$ and $s_j$, respectively. Then, this metric can be written as

$$\langle s_i, s_j \rangle_{cc} = \frac{max\left|F_2^{-1}\{S_i S_j^*\}\right|}{\sqrt{max\left|F_2^{-1}\{S_i S_i^*\}\right| max\left|F_2^{-1}\{S_j S_j^*\}\right|}}$$

where $F_2^{-1}\{...\}$ is the 2D inverse Fourier transform and $S_j^*$ is the complex conjugate of $S_j$. By construction, one has $0 \leq \langle s_i, s_j \rangle_{cc} \leq 1$.

The remaining three metrics were constructed from the notion of total power. Parseval's theorem is

$$\int_{-\infty}^{\infty} |s(t)|^2 dt = \int_{-\infty}^{\infty} |S(f)|^2 df$$

which states that the total power can be computed in either the time domain or the frequency domain. Let $s_i \circ s_j$ represent the element-by-element matrix multiplication of the slices $s_i$ and $s_j$. The first metric based on total power can be written as

$$\langle s_i, s_j \rangle_1 = \frac{\left| \sum s_i \circ s_j \right|}{\sqrt{\sum s_i \circ s_i \sum s_j \circ s_j}}$$

where $\sum s_i \circ s_j$ represents the summation of the elements of the matrix. The normalization is again such that $0 \leq \langle s_i, s_j \rangle_1 \leq 1$. For real-valued data, when $i = j$, the numerator in $\langle s_i, s_j \rangle_1$ is essentially a discrete representation of the left-hand-side of Parseval's theorem (i.e., $|s|^2 = s^2$) averaged over an angular swath. That is, the summation over time is a measure of total power and the summation over angular swath gives the total power in the slice of data. When the slices of data are different, then elements of $s_i \circ s_j$ may be negative and in fact the summation may be negative.

For the right-hand-side of Parseval's theorem, the real-valued data are Fourier transformed from the time domain into the frequency domain. This results in complex-valued signals and one has $|S|^2 = |S||S|$. Let $|S_i| \circ |S_j|$ represent the element-by-element multiplication of the absolute values of the elements of $S_i$ and $S_j$. The second metric becomes

$$\langle s_i, s_j \rangle_2 = \frac{\sum |S_i| \circ |S_j|}{\sqrt{\sum |S_i| \circ |S_i| \sum |S_j| \circ |S_j|}}$$

with the summation indicating that all elements are to be summed (i.e., an angular average of a frequency-domain estimate of the total power in a slice).

The third and final metric utilized complex-valued time signals. Let $c_i$ be the complex-valued signal associated with $s_i$. $c_i$ may be obtained from a Hilbert transform, which is often applied to generate the envelop of a time signal. This metric has the form

$$\langle s_i, s_j \rangle_3 = \frac{\sum |c_i| \circ |c_j|}{\sqrt{\sum |c_i| \circ |c_i| \sum |c_j| \circ |c_j|}}$$

As in previous metrics, the summation in $\langle s_i, s_j \rangle_3$ represents a summation over both time and angle. This is then again a measure of the total power in a slice.

D.  Model-Model Comparisons

When comparing the predictions of models, it is assumed that the same scattering scenario has been modeled (i.e., the same environment, target, and scattering geometry). The comparison can be between distinct independent models (e.g., TIER and PC-SWAT) or a single model executed with limits on the included physics. In the former, one is trying to assess whether the independent models capture the same observables. That is, the target signature produced by one model should largely agree with the target signature produced the other. In the latter, one is often seeking to isolate the physics associated with an observable (e.g., rigid response versus elastic response). In the following comparisons, the TIER model is used with various limits on the included physics.

The first model-model comparison used the full target response of those listed in Table 7. Figure 3 shows the four metrics for targets at a 10-m horizontal range, where the 9×9 grid in each panel delineates the nine target rotations. Figure 3a corresponds to the 2D cross-correlation metric, which by its very nature forces the "best" alignment of the data. The main diagonal is the auto-correlation of $s_i$. The panels b - d are for the metrics associated with total power, and here the main diagonal is similar to the auto-correlation in that $s_i$ is compared to itself. It is found that each panel contains prominent sub-diagonals. These sub-diagonals reveal that a slice of data for one target appears to be the same as a slice from a different target.

The second model-model comparison involved the free-field scattering from a target versus a proud target. That is, the TIER model included only the direct path for free-field scattering response; while it included the direct path and 3 paths associated with interaction with the water-sediment interface for a proud target. The targets of Table 7 were placed at a 25 m horizontal range from a linear SAS path. Inspection of Figure 4 reveals that inclusion of only the direct path captures some of the response for a proud target (i.e., prominent diagonal lines). This might be anticipated as the bottom interacting paths in the proud response are delayed in time with respect to the direct path and only interfere with the direct path's trailing contribution. Figure 4 suggests that $\langle s_i, s_j \rangle_3$ may provide better discrimination of the targets than the other metrics.

The third model-model comparison decomposed the full target response into a rigid component and an elastic component. The rigid component is typically associated with specular/geometrical scattering, and an elastic response is associated with elastic modes of oscillation of the target. The four metrics are displayed in Figure 5.

E.  Model-Data Comparisons

The four metrics were applied to the TREX13 data listed in Table 6 and TIER simulated target responses for targets in Table 7. Examples of the metrics are displayed in Figure 6 for targets at a 10 m horizontal range. For these comparisons, the TREX13 targets were tgt09, tgt11, tgt17, tgt20, and tgt21; while TIER simulations for all targets listed in Table 7 were performed. Inspection of Figure 6 suggests that the conventional 2D cross-correlation metric, $\langle s_i, s_j \rangle_{cc}$, performs better than the other metrics although $\langle s_i, s_j \rangle_3$ does exhibit some sub-diagonals in the TIER versus TREX data regions. This result may be expected as $\langle s_i, s_j \rangle_{cc}$ by construction aligns the data and model result and selects only the maximum value in the magnitude of the slices; while the other metrics implicit assume an alignment.
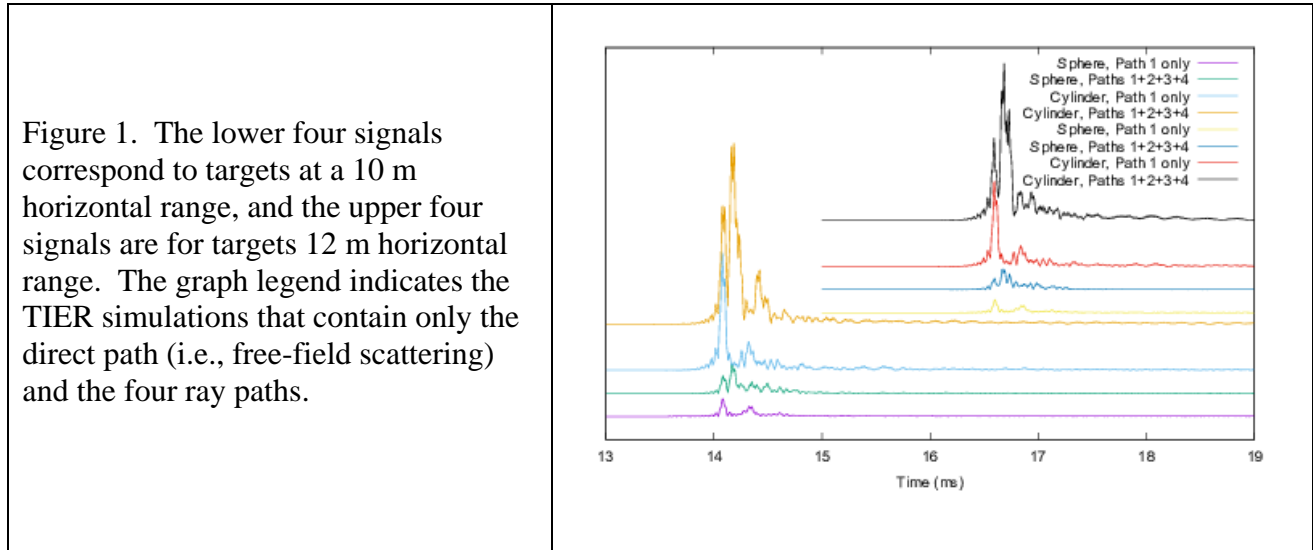
**IMPACT/APPLICATIONS**

Four metrics were investigated. The metric, based on 2D cross-correlation, is typically used in classification algorithms. Model-model comparisons suggest the other metrics, based on total power, have a potential to provide alternative computational kernels for classifiers. Applying the same four metrics to the model-data comparisons demonstrate that uncertainty in the experimental data necessitates an alignment of data in both the time and target-centered angle domains.
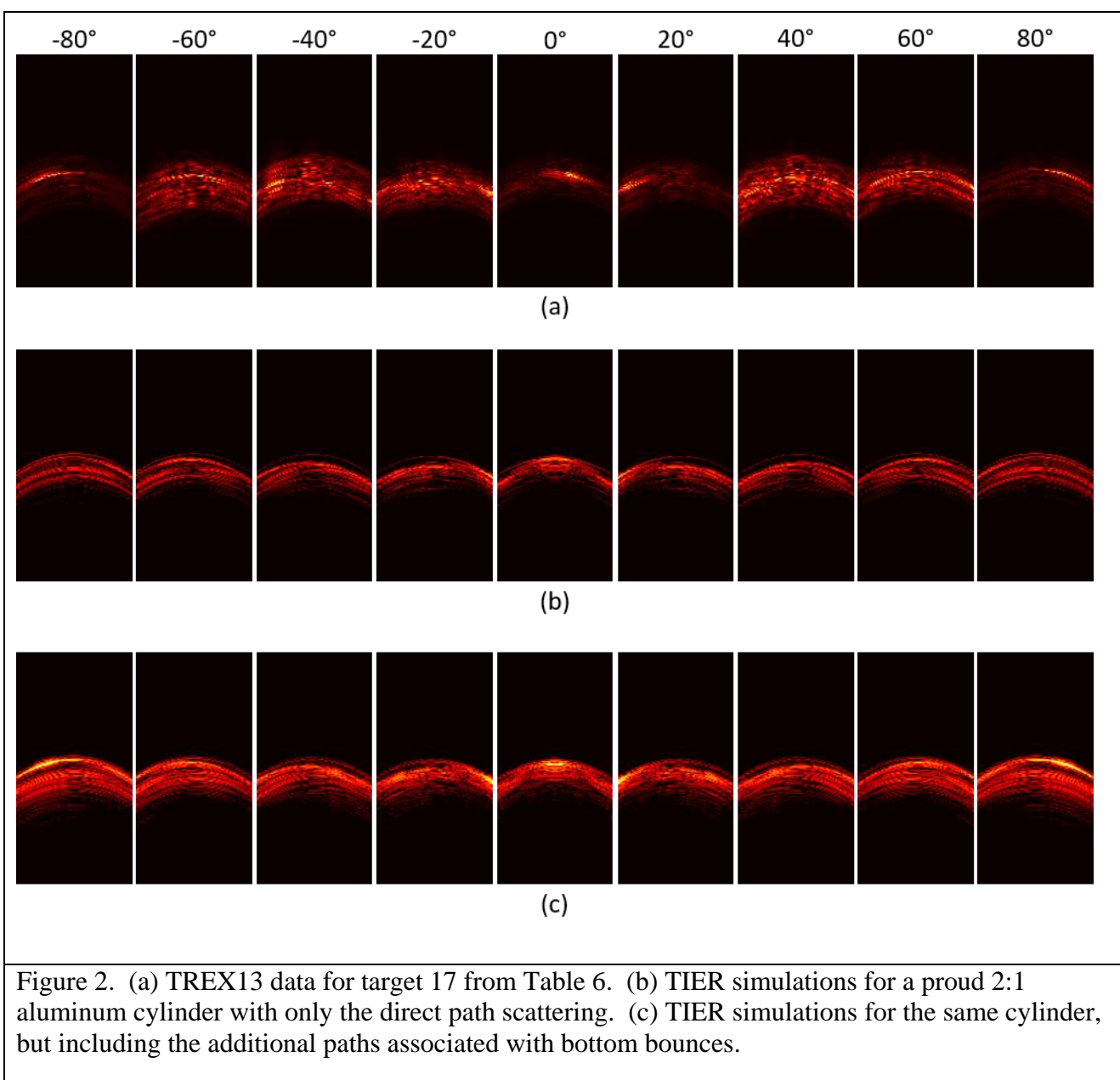
For $n$ slices of data, $\langle s_i, s_j \rangle_{cc}$ requires $n! + n$ 2D Fourier transforms to be computed. The frequency-domain total power metric, $\langle s_i, s_j \rangle_2$, requires only $n$ Fourier transforms of the time domain data. The time-domain metric, $\langle s_i, s_j \rangle_3$, requires $2n$ Fourier transforms to obtain complex-valued

signals. Finally, the simplest metric, $\langle s_i, s_j \rangle_1$, requires only an element-by-element matrix multiplication, which translates to a significant reduction of computational cost.

**RELATED PROJECTS**

The Performance Estimate (PE) program is a multi-institutional effort with participants from APL-UW, ARL-PSU, GTRI, and NSWC-PC. The goal of this effort is to establish procedures to assess the overall performance of a classification chain. Although the TIER model has been used to generate nearly 2 TB of data for the PE program, the metrics investigated here have yet to be integrated into a (RVM or SVM) classifier.

Figure 1. The lower four signals correspond to targets at a 10 m horizontal range, and the upper four signals are for targets 12 m horizontal range. The graph legend indicates the TIER simulations that contain only the direct path (i.e., free-field scattering) and the four ray paths.

Figure 2. (a) TREX13 data for target 17 from Table 6. (b) TIER simulations for a proud 2:1 aluminum cylinder with only the direct path scattering. (c) TIER simulations for the same cylinder, but including the additional paths associated with bottom bounces.
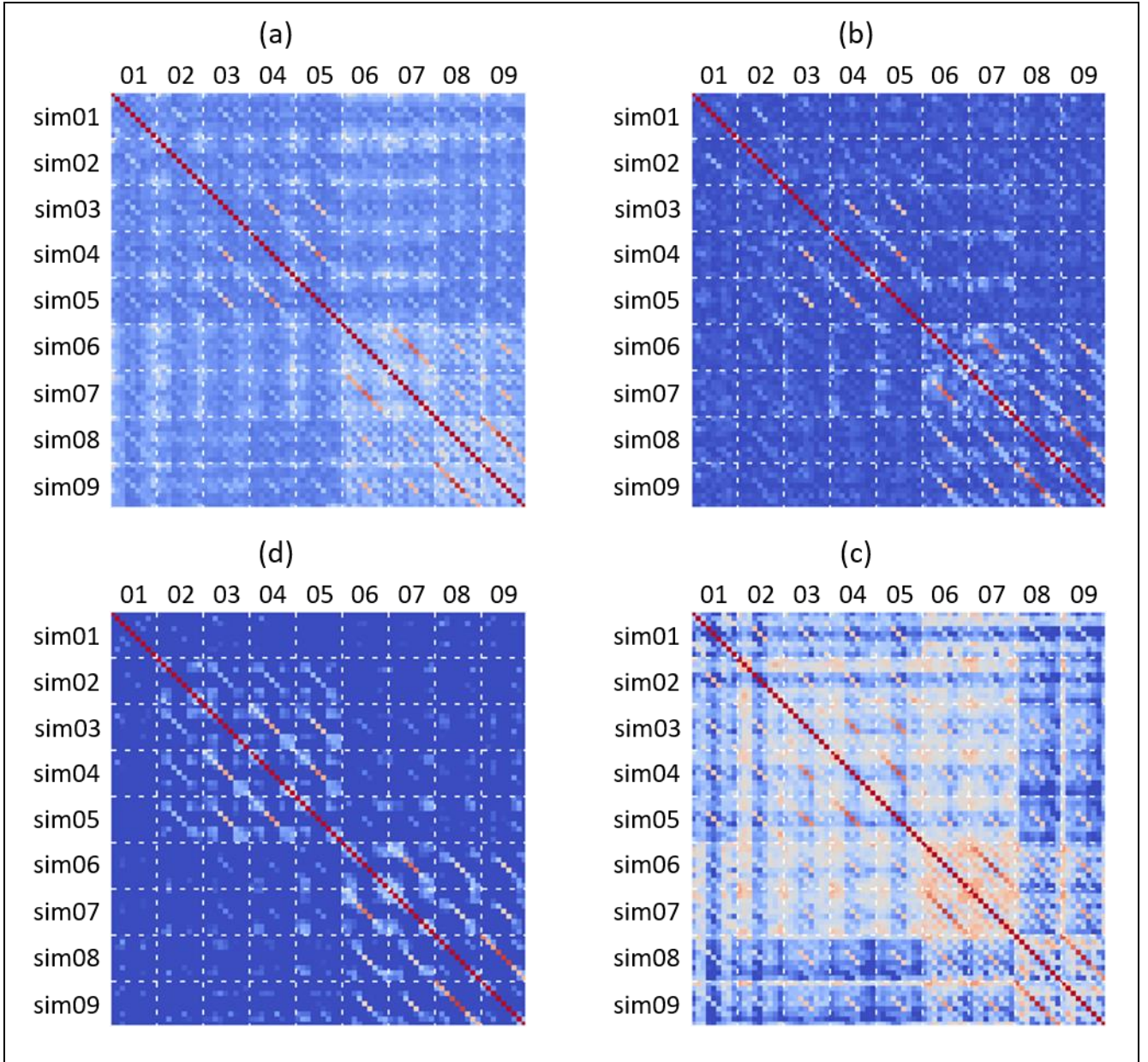
Figure 3. The results of the four metrics applied to the full target response with the targets at a 10 m horizontal range. (a) $\langle s_i, s_j \rangle_{cc}$, (b) $\langle s_i, s_j \rangle_1$, $\langle s_i, s_j \rangle_2$, and (d) $\langle s_i, s_j \rangle_3$. The 01-09 labeling above each coincides with sim01-sim09.

Figure 4: Model-model comparison of scattering from a proud target (P1234) and a target in the free field (P1). The targets were placed at a 25 m horizontal range. The panels correspond to (a) $\langle s_i, s_j \rangle_{cc}$, (b) $\langle s_i, s_j \rangle_1$, (c) $\langle s_i, s_j \rangle_2$, and (d) $\langle s_i, s_j \rangle_3$.
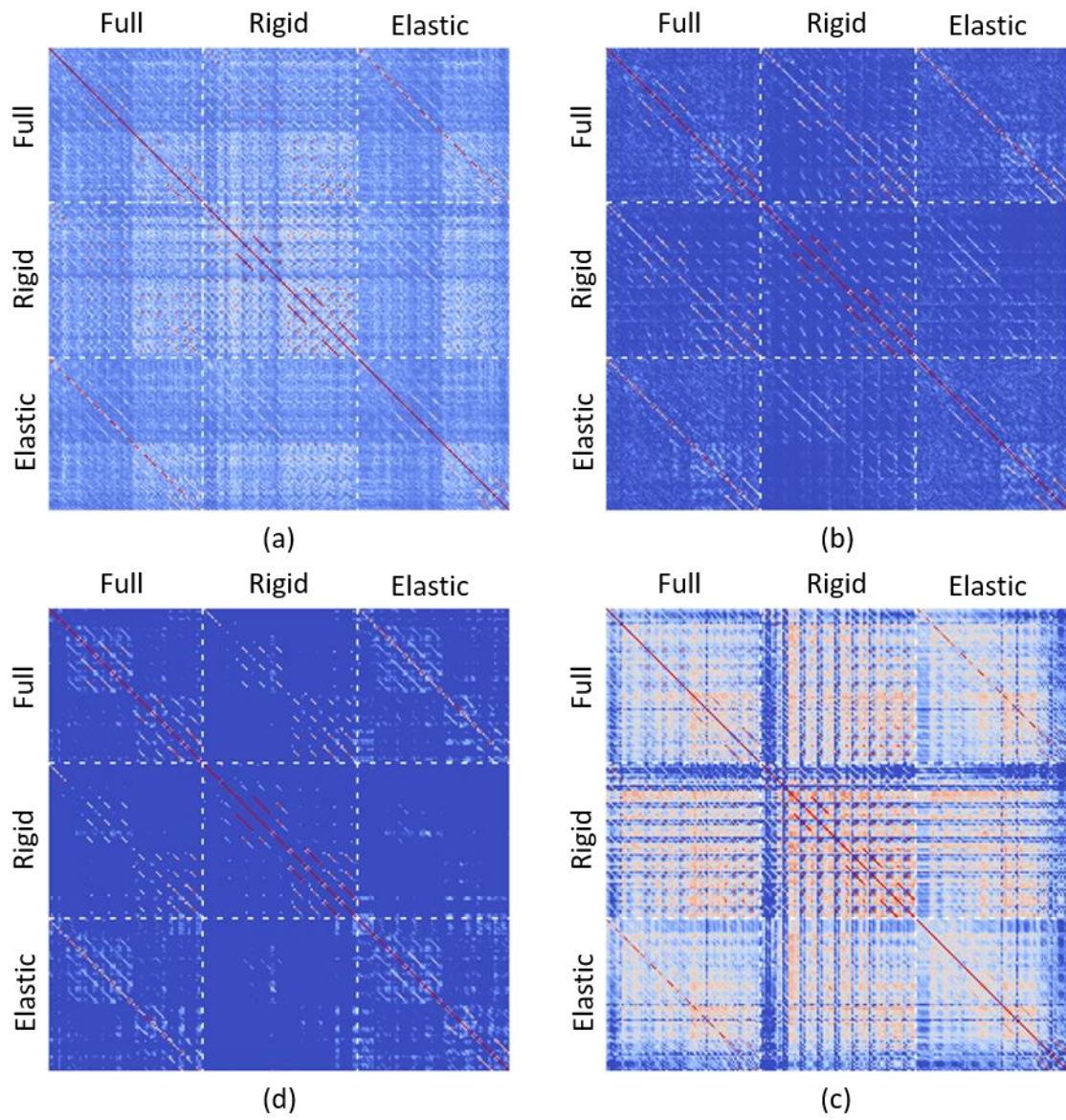
Figure 5: Model-model comparison for a decomposition of the full target response into a rigid component and an elastic component. The targets were proud on a sand sediment interface at a 20 m horizontal range. The panels correspond to (a) $\langle s_i, s_j \rangle_{cc}$, (b) $\langle s_i, s_j \rangle_1$, (c) $\langle s_i, s_j \rangle_2$, and (d) $\langle s_i, s_j \rangle_3$.
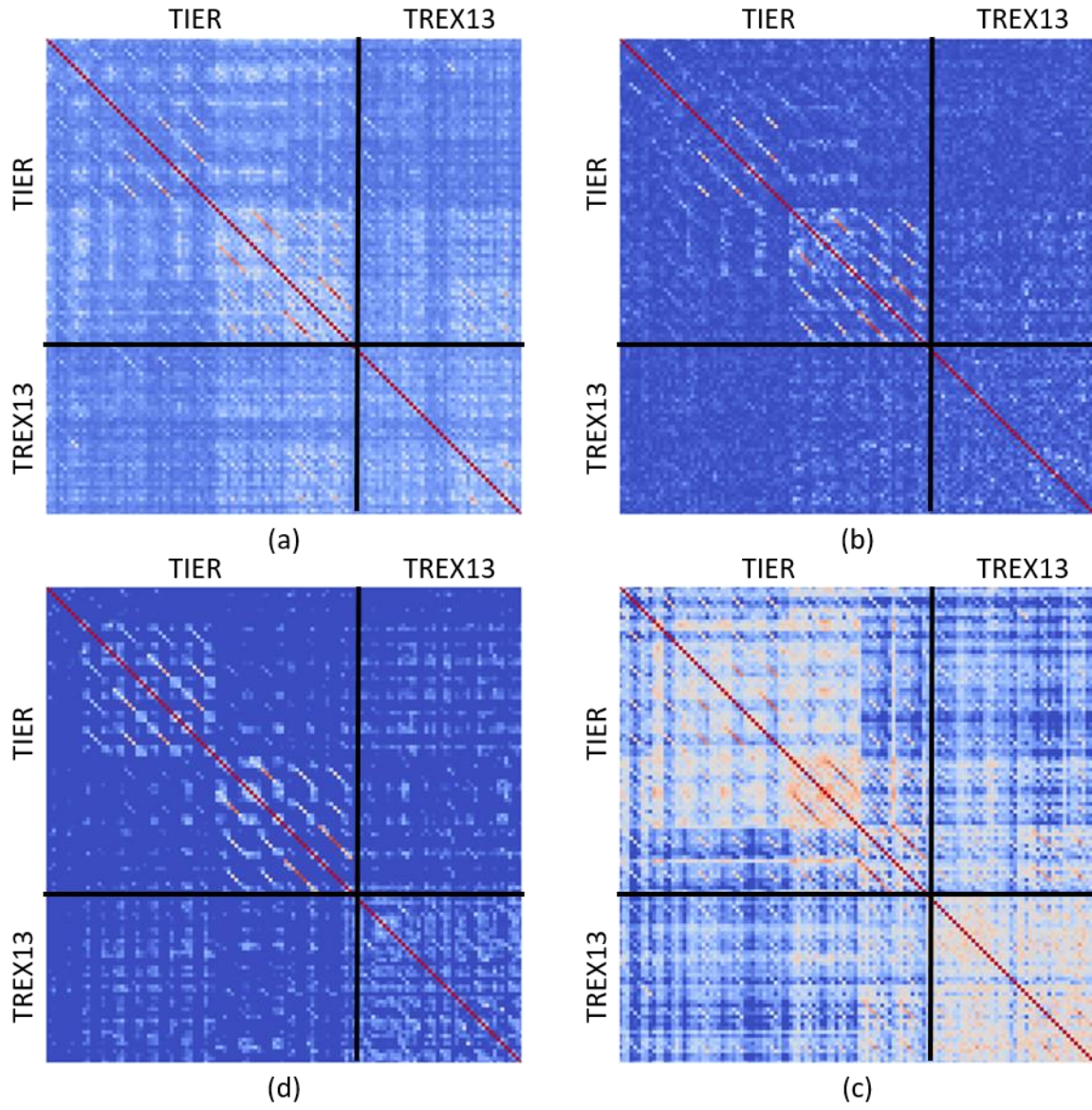
Figure 6: Model-data comparison for TREX13 data and TIER model results. The targets were proud on a sand sediment interface at a nominal horizontal range of 10 m. The panels correspond to (a) $\langle s_i, s_j \rangle_{cc}$, (b) $\langle s_i, s_j \rangle_1$, (c) $\langle s_i, s_j \rangle_2$, and (d) $\langle s_i, s_j \rangle_3$.

# REPORT DOCUMENTATION PAGE

The public reporting burden for this collection of information is estimated to average 1 hour per response, including the time for reviewing instructions, searching existing data sources, gathering and maintaining the data needed, and completing and reviewing the collection of information. Send comments regarding this burden estimate or any other aspect of this collection of information, including suggestions for reducing the burden, to Department of Defense, Washington Headquarters Services, Directorate for Information Operations and Reports (0704-0188), 1215 Jefferson Davis Highway, Suite 1204, Arlington, VA 22202-4302. Respondents should be aware that notwithstanding any other provision of law, no person shall be subject to any penalty for failing to comply with a collection of information if it does not display a currently valid OMB control number.
**PLEASE DO NOT RETURN YOUR FORM TO THE ABOVE ADDRESS.**

| 1. REPORT DATE *(DD-MM-YYYY)* | 2. REPORT TYPE | 3. DATES COVERED *(From - To)* |
|---|---|---|

**4. TITLE AND SUBTITLE**

**5a. CONTRACT NUMBER**

**5b. GRANT NUMBER**

**5c. PROGRAM ELEMENT NUMBER**

**6. AUTHOR(S)**

**5d. PROJECT NUMBER**

**5e. TASK NUMBER**

**5f. WORK UNIT NUMBER**

**7. PERFORMING ORGANIZATION NAME(S) AND ADDRESS(ES)**

**8. PERFORMING ORGANIZATION REPORT NUMBER**

**9. SPONSORING/MONITORING AGENCY NAME(S) AND ADDRESS(ES)**

**10. SPONSOR/MONITOR'S ACRONYM(S)**

**11. SPONSOR/MONITOR'S REPORT NUMBER(S)**

**12. DISTRIBUTION/AVAILABILITY STATEMENT**

**13. SUPPLEMENTARY NOTES**

**14. ABSTRACT**

**15. SUBJECT TERMS**

| 16. SECURITY CLASSIFICATION OF: | | | 17. LIMITATION OF ABSTRACT | 18. NUMBER OF PAGES | 19a. NAME OF RESPONSIBLE PERSON |
|---|---|---|---|---|---|
| a. REPORT | b. ABSTRACT | c. THIS PAGE | | | |
| | | | | | 19b. TELEPHONE NUMBER *(Include area code)* |